npj | Flexible Electronics

www.nature.com/npjflexelectron

ARTICLE OPEN

Check for updates

Stretchable transparent electrodes for conformable wearable organic photovoltaic devices

Nan Cui[1,2], Yu Song[1,2], Ching-Hong Tan[1], Kai Zhang[1], Xiye Yang[1], Sheng Dong[1], Boming Xie[1] and Fei Huang[1]✉

To achieve adhesive and conformable wearable electronics, improving stretchable transparent electrode (STE) becomes an indispensable bottleneck needed to be addressed. Here, we adopt a nonuniform Young's modulus structure with silver nanowire (AgNW) and fabricate a STE layer. This layer possesses transparency of >88% over a wide spectrum range of 400–1000 nm, sheet resistance below 20 Ω sq^{-1}, stretchability of up to 100%, enhanced mechanical robustness, low surface roughness, and good interfacial wettability for solution process. As a result of all these properties, the STE enables the fabrication of a highly efficient ultraflexible wearable device comprising of both organic photovoltaic (OPV) and organic photodetector (OPD) parts with high mechanical durability and conformability, for energy-harvesting and biomedical-sensing applications, respectively. This demonstrates the great potential of the integration of OPVs and OPDs, capable of harvesting energy independently for biomedical applications, paving the way to a future of independent conformable wearable OPV/OPDs for different applications.

npj Flexible Electronics (2021)5:31 ; https://doi.org/10.1038/s41528-021-00127-7

INTRODUCTION

Wearable organic photovoltaics (WOPVs) for self-powered electronic skins, human–machine interactions (HMIs), real-time health monitoring, internet of things (IoTs) require a strong and comfortable adhesion that adapts to the complexity of human's skin movement without compromising their performance and lifetime[1–4]. Devices that can conform to the skin surface seamlessly would provide an accurate and precise measurement of any physiological signal of interest[5]. Numerous studies on flexible transparent electrodes have achieved mechanical bending durable OPV devices with performance comparable to indium tin oxide (ITO) analogs[6–8]. Among different flexible transparent electrodes[7,9–16], silver nanowires (AgNWs) are perceived as the promising alternative for flexible OPV devices owing to some of its remarkable properties such as low percolation threshold, superior transparency, high electrical conductivity, and excellent flexibility[17]. Nonetheless, AgNW electrodes suffer from several shortcomings, such as high surface roughness and poor adhesion to substrates, leading to severe leakage current and poor mechanical robustness[18]. To improve device conformation to skin irregular surface stretches for portable and WOPV devices, the development of stretchable transparent electrodes (STEs) which utilizes a soft substrate as an interface between the device and human skin is of particular interest. Recently, the incorporation of grid-like AgNW electrode on the plastic polyethylene terephthalate (PET) substrates is shown to lower the surface roughness for highly efficient flexible single-junction and tandem OPV device[2]. The combination AgNW/PET device is also exhibited to have high bending durability at a bending radius of 3 mm and retained >90% of its initial efficiency after 1000 bending cycles[19]. These studies independently indicate the importance of the integration between AgNW and the underlying substrate to have a better adhesion for a highly robust WOPV device[2,10,19]. However, the plastic polymer substrates, such as PET, polyethylene naphthalate (PEN), perylene, and polyimide (PI)[3,20] applied in these OPV devices, possessing Young's moduli of 2.8–6.1 GPa[21], are unable to utilize the stretchability of the AgNW network. While reports have shown that AgNWs integrated with more elastic polymers such as polydimethylsiloxane (PDMS), polyurethane (PU), and polyurethane acrylate (PUA), which have a similar Young's modulus to the human body, enable the network to withstand a large stretchability of over 50%[22–25], the poor chemical stability of the elastic polymer substrate remains a huge challenge for high-performance WOPV devices using AgNW-based STEs. To improve the chemical stability of the polymer, a lamination strategy was introduced that avoids the direct contact of chemical reagents, but this creates a high contact resistance, leading to a poor performance of the organic thin-film devices[26]. Other than focusing on the conformability of a substrate, the tensile strength has been shown to be one of the important indicators for the mechanical robustness and durability of the materials[27].

Organic photodetectors (OPDs) with a near-infrared (NIR) absorbing bulk-heterojunction (BHJ) configuration on the other hand, has also attracted increasing attention for their potential in biomedical wearable electronic application[5,28,29]. In particular, NIR can play a prominent role in biomedical and clinical applications due to the deep penetration depth of NIR photons transmitting beyond the skin surface, making the high transparency of AgNW-based STE in the NIR region an appealing component in wearable OPDs (WOPDs) for biomedical sensing[30]. However, the demonstration of such conformable WOPDs based on AgNW electrodes has been scarce for biological sensing. To meet the requirements for wearable application, the electrode should achieve several vital features simultaneously: excellent conductivity and high transparency that are crucial for device performance; mechanical deformability/stretchability and robust flexibility for maintaining continuous conducting paths in dynamic operating environment; good chemical stability, and wettability for low-cost solution process; smooth surface for decreasing contact resistance and avoiding large leakage current[2,17,21,31].

Here, we demonstrate the fabrication of AgNW-based STEs using a nonuniform Young's modulus structure. The nonuniform

[1]Institute of Polymer Optoelectronic Materials and Devices, State Key Laboratory of Luminescent Materials and Devices, South China University of Technology, 510640 Guangzhou, People's Republic of China. [2]These authors contributed equally: Nan Cui, Yu Song. ✉email: msfhuang@scut.edu.cn

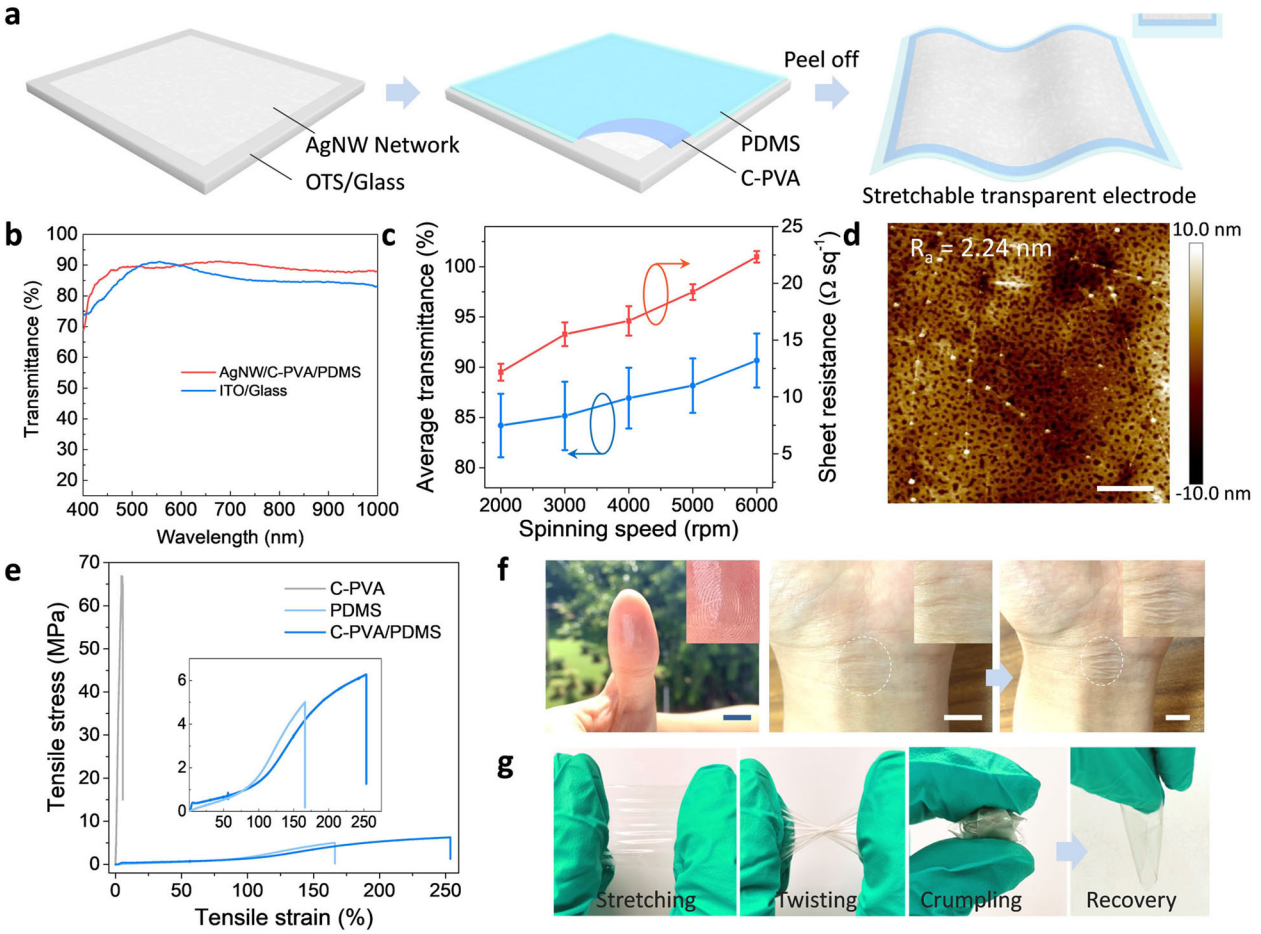

Fig. 1 Stretchable transparent electrode with nonuniform Young's modulus polymer structure. a Schematic illustration of the fabrication process for AgNW/C-PVA/PDMS electrode. The inset is the section view of the embedded AgNW/C-PVA/PDMS electrode. **b** Optical transmittance of stretchable AgNW/C-PVA/PDMS and commercial rigid ITO/glass electrodes. **c** Average transmittance at a wavelength ranging from 400 to 1000 nm and sheet resistance of AgNW-based electrodes as a function of spinning speed. Error bars represent the standard deviation. **d** AFM image of embedded AgNW/C-PVA/PDMS electrode with surface roughness of 2.24 nm. Scale bar is 1 μm. **e** Typical mechanical testing curves of C-PVA, PDMS, and C-PVA/PDMS under tensile strain. **f** Photographs of AgNW/C-PVA/PDMS electrodes conformed onto thumbprint and the moving wrist. Scale bar is 1 cm. **g** Photographs of AgNW/C-PVA/PDMS electrodes withstanding various deformations of stretching, twisting, crumpling, and recovery after deformations.

Young's modulus structure endows the STEs with enhanced mechanical durability and tensile strength, high chemical stability, and improved interfacial wettability for the organic active layers. The obtained electrode shows a sheet resistance below 20 Ω sq^{-1}, transparency of >88% (including the substrate), surface roughness of 2.24 nm, and a stretchability of up to 100%, all of which meet the basic requirements for a wearable electronic application. The WOPV device fabricated using said STE achieved performance comparable to its traditional rigid ITO-based counterpart and maintained >96% of the initial power conversion efficiency (PCE) after 4000 bending cycles at an extreme bending radius of 0.5 mm, indicating excellent mechanical stability. The WOPD which adopts the same device structure and STE demonstrates a successful heart rate detection for biomedical application. Altogether, the study herein illustrates the potential of AgNW-based STE for conformal dual-purpose WOPD biomedical sensing and WOPV energy-harvesting devices.

RESULTS AND DISCUSSION

STE with nonuniform Young's modulus structure

The procedure for fabricating the STE with nonuniform Young's modulus structure is schematically displayed in Fig. 1a. AgNW network was fabricated onto an octadecyltrichlorosilane-modified glass (OTS/glass) via spin-coating. The OTS modification provides a low surface-energy interface[32], which is beneficial for the subsequent mechanical peeling processes to obtain an embedded STE. Cross-linked polyvinyl alcohol (C-PVA) and PDMS were successively applied onto AgNW network to form a bilayer polymer substrate forming a nonuniform Young's modulus matrix by the spin-coating process. Owing to the good mechanical stretchability and biocompatibility of PDMS, it has been widely utilized in skin-like and wearable electronics[33]. However, PDMS is hardly compatible with common organic solvent due to its poor chemical resistance and is a non-preferred solvent in the manufacturing process of various chemical treatments. C-PVA adopted here has been demonstrated with the advantages of flexibility, transparency, ultrathin, and biocompatibility in the previous reports[34]. Moreover, C-PVA is solvent-resistant, which remedies the shortage of PDMS. Finally, the whole electrode structure, including AgNW network, C-PVA, and PDMS, was easily peeled off from the OTS/glass and flipped over to form a STE. The upper right inset of Fig. 1a shows that the AgNW network is embedded in the nonuniform Young's modulus polymer matrix composed of flexible C-PVA and elastic PDMS. The ultrathin C-PVA film acts as the buffer layer located between AgNW conductive

layer and hydrophobic PDMS. The AgNW/C-PVA/PDMS electrode, employing the embedded structure, is coplanar and flat. The fabrication process for STE is simple and feasible, indicating a great potential for all-solution, low-cost fabrication.

Due to the excellent transparency of all the components (AgNW network, C-PVA, and PDMS) within the STE structure, the prepared electrode including the soft substrate presents an average transmittance (T_{avg}) of 88%, over the wide range of 400–1000 nm (Fig. 1b). Compared to commercial rigid transparent ITO electrode (T_{avg} of 85%) on glass, the stretchable transparent AgNW/C-PVA/PDMS electrode shows higher transparency, especially in the wavelength range of 600–1000 nm. Due to high tissue transparency in the NIR region, the stretchable transparent AgNW/C-PVA/PDMS electrode is promising for biological applications that require, in addition to high conformability, transparency in the NIR wavelength region[35]. As shown in Fig. 1c, the optical transparency and electrical properties of AgNW-based electrodes can be tuned by modulating the spinning speed. The sheet resistance (R_s) of AgNW network prepared by spin-coating at 2000 rpm was $12.2 \pm 0.7\ \Omega\ sq^{-1}$ with T_{avg} of $84.2 \pm 3.1\%$. When the spinning speed increased to 6000 rpm, the average transmittance and sheet resistance increased up to $90.7 \pm 2.7\%$ and $22.3 \pm 0.5\ \Omega\ sq^{-1}$, respectively. Along with the increase of spinning speed, both thickness and AgNW area coverage decreased, and the resulted sparse network led to the increase of transmittance and sheet resistance. The thickness of the AgNW network obtained by different spinning speed can be found in Supplementary Table 1. The superior electrical conductivity and optical transparency of AgNW/C-PVA/PDMS which are comparable to the performances of commercial rigid ITO are much higher than those of CNTs and graphene reported[36], indicating the application capability of stretchable transparent AgNW-based electrode in wearable optoelectronic devices. Considering the integration of AgNW-based STE into thin-film devices, surface roughness is another important factor that affects the device's performance. The atomic force microscope (AFM) image in Fig. 1d presents that the surface roughness of AgNW/C-PVA/PDMS is 2.24 nm. The flat and smooth surface avoids severe leakage current caused by protruding nanowires in organic thin-film devices for the active layer of ~100 nm thickness. It is noteworthy that the voids within AgNW network are filled with C-PVA, which may enhance the adhesion and tightness at the wire–wire junctions, and prevent PDMS from directly contacting with organic solvents.

To investigate the mechanical properties of the polymer matrix, the tensile tests of C-PVA, PDMS, and C-PVA/PDMS were performed as illustrated in Fig. 1e. C-PVA with a high Young's modulus of 1.3 GPa possesses a high tensile strength of 64.6 MPa, but poor stretchability with the elongation at break occurring at only 5.5% tensile strain; PDMS with a low Young's modulus of 2.8 MPa has a stretchability up to 165%, but a low tensile strength of 4.8 MPa. Elongation at break is defined as $(L_f - L_0)/L_0(100\%)$, where L_0 and L_f represent the original length and the length at the break, respectively. In comparison with pristine C-PVA and PDMS, the mechanical properties of combined C-PVA/PDMS have been prominently improved. The tensile strength and elongation at break of C-PVA/PDMS were 6.3 MPa and 252%, which increased 25% and 51.8% to that of PDMS. Obviously, C-PVA/PDMS hybrid polymer matrix with the nonuniform Young's modulus structure makes up for the mechanical deficiency of C-PVA and PDMS. The cause may be that during the large tensile strain, amounts of impact energy on C-PVA/PDMS is dissipated by the cracks that occurred in C-PVA, which in turn improves the impact strength of the hybrid material. The optical images of C-PVA/PDMS under different tensile strains can be found in Supplementary Fig. 1. Despite the distinctly enhanced mechanical tensile strength of the hybrid polymer, Young's modulus of C-PVA/PDMS (2.9 MPa) is still much approximate to PDMS (2.8 MPa). The low Young's modulus is beneficial for realizing the soft conformal contact with expandable skins, tissues, and organs of the human being for bio-integrated electronic applications[37]. As can be seen in Fig. 1f, g, the STEs could be conformally coupled onto the human skin and kept seamless contact with the thumbprint and the wrinkled skin by Van der Waals force. Due to the high transparency, the STEs can also serve for invisible wearable electronics with esthetics. The enhanced mechanical properties make the electrode withstand various deformations, such as stretching, twisting, and crumpling. Due to the stress relief in a bilayer structure, the AgNW/C-PVA/PDMS electrode is able to recover from the crumpling without mechanical damage, which contributes greatly to effective manipulation during practical application. This strategy provides a simple and efficient approach by recombining the advantages of PDMS and C-PVA into the STE with a double-layered scheme, and achieves the polymer matrix combined high tensile strength and low Young's modulus.

Furthermore, the electrical properties of flexible electrodes were evaluated under mechanical deformations. Figure 2a compares the electrical resistance changes of ITO/PET, AgNW/PDMS, and AgNW/C-PVA/PDMS electrodes under different outcurve-bending radii (r). For commercial flexible ITO/PET electrode, the relative change in resistance increased dramatically with bending radius decreased below 5 mm due to its brittle nature, whereas the conductivity of AgNW-based electrodes remained relatively stable even at the extremely small radius of 0.2 mm. Long-term reliability under cyclic mechanical stress is of great significance for the practical use of flexible electrodes. Taking this into account, the real-time bending measurement was conducted in Fig. 2b. At a constant bending radius of 5 mm, the AgNW-based embedded electrodes can withstand more than 4000 bending cycles without noticeable resistance variation. However, the resistance of ITO/PET had increased about ~40 times to its original resistance after the cyclic bending. The inset provides the partially enlarged views of the curves for AgNW/PDMS and AgNW/C-PVA/PDMS. The resistance dynamic range of AgNW/C-PVA/PDMS was much smaller than that of AgNW/PDMS during cyclic bending, indicating the positive effect of C-PVA interlayer for mechanical robustness and stability. Figure 2c, d also shows the beneficial effects of the C-PVA interlayer on the mechanical stretchability of the STEs. Figure 2c illustrates the measured resistance change of embedded AgNW/PDMS and AgNW/C-PVA/PDMS as a function of increasing tensile strain. The AgNW/PDMS showed a significant increase in resistance with the strain increasing over 40% in comparison with AgNW/C-PVA/PDMS electrode. During the cyclic stretch-release test employing 0–20% tensile strain, the resistance variation of AgNW/PDMS continuously increased as more cycles were completed (Fig. 2d). Clearly, the conductivity of AgNW/C-PVA/PDMS hold relatively stable during 4000 cycles of deformation, indicating good mechanical stability during the stretching and releasing cycles. As mentioned above, the hybrid C-PVA/PDMS polymer substrate showed better tensile strength than PDMS. The poor stability of AgNWs/PDMS electrodes may origin from the low strength of PDMS and vastly mismatched Young's modulus between AgNW and PDMS. The ultrathin flexible C-PVA of 270 nm adopted here serving as an effective buffer layer between AgNW and PDMS due to the moderate Young's modulus value between metallic materials and elastic polymer. Besides, the conductivity of the AgNW/C-PVA/PDMS electrodes did not decay at all even after conducting 50 tape tests without exfoliation (Supplementary Fig. 2), indicating the strong adhesion between PDMS and C-PVA thin films by noncovalent bonding. In Fig. 2e, the stretchable transparent AgNW/C-PVA/PDMS electrode, serving as the interconnectors of a yellow commercial LED, presents excellent conductivity under different tensile strains. During the stretching of the AgNW/C-PVA/PDMS interconnectors, the yellow LED showed bright yellow light, indicating the outstanding mechanical stretchability and good conductivity of the AgNW/C-PVA/PDMS conductor. The LED could be lit up even at the tensile

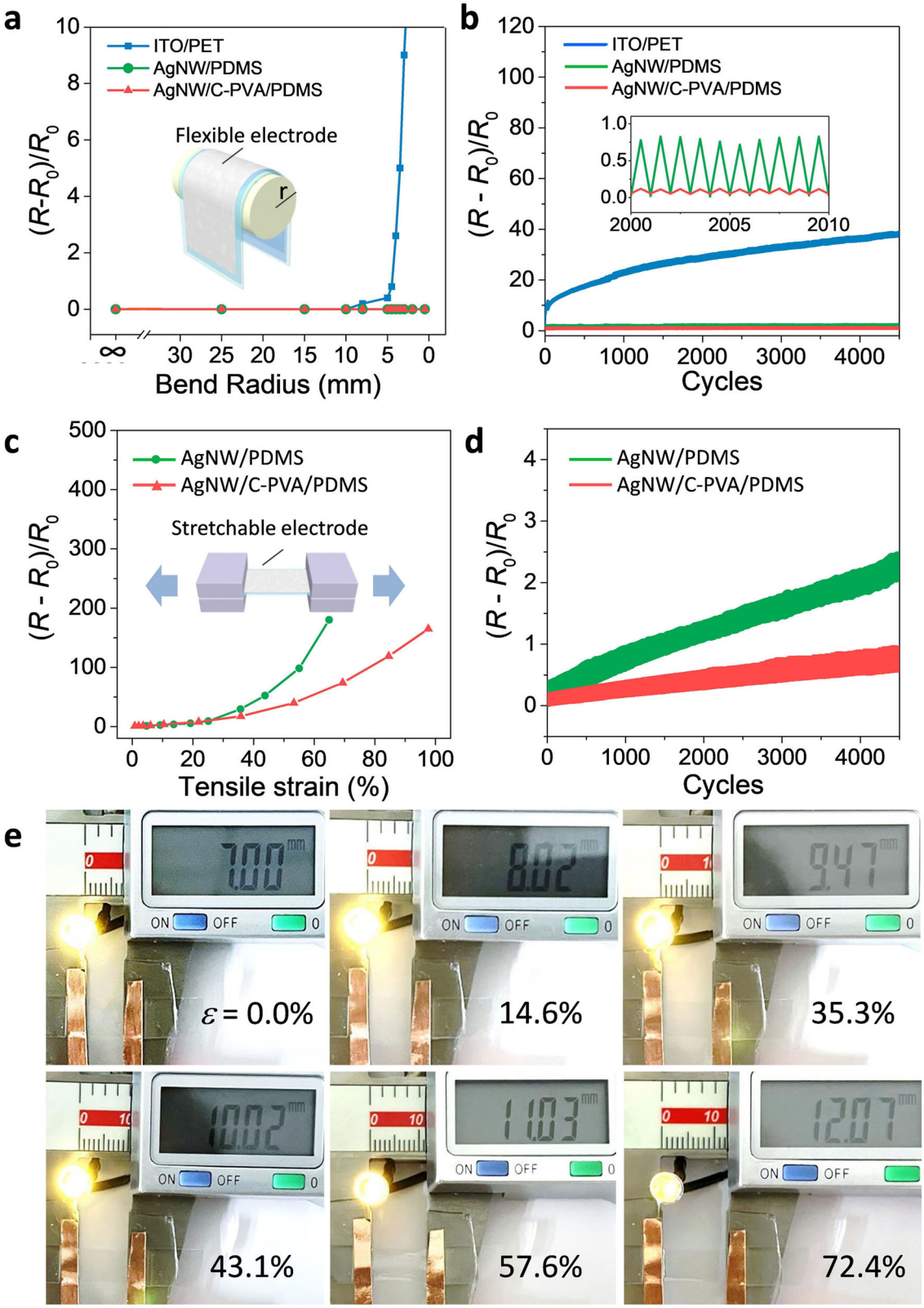

Fig. 2 Electrical properties of flexible electrodes under various mechanical strains. a Relative changes in resistance ($(R - R_0)/R_0$) of ITO/PET, AgNW/PDMS, and AgNW/C-PVA/PDMS versus different bending radii (r) and (**b**) bending cycles at a bending radius of 5 mm. Where R is the resistance of the flexible electrode under strain, and R_0 represents the original resistance. The inset is the magnified region of relative resistance change under cyclic bending. **c** Relative resistance changes of AgNW/PDMS and AgNW/C-PVA/PDMS electrodes versus tensile strain and (**d**) cyclic tensile stretching and releasing between 0 and 20% strains. **e** AgNW/C-PVA/PDMS interconnections connected to commercial yellow LEDs with different tensile strains (ε).

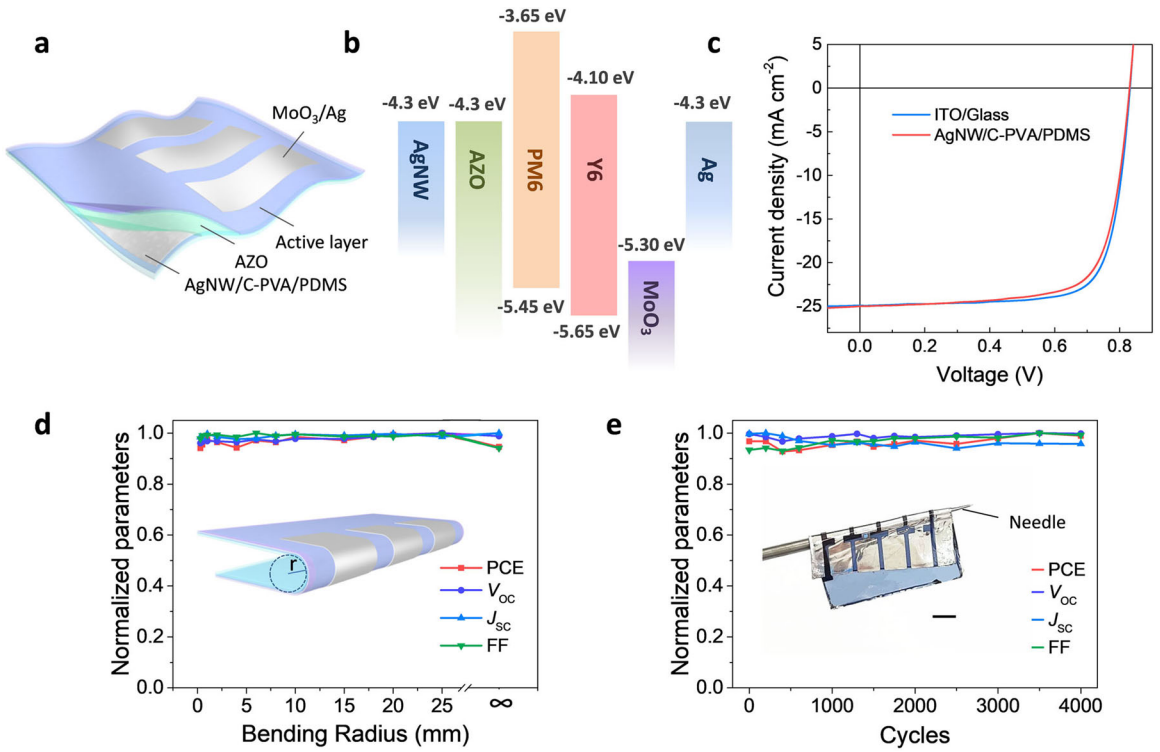

Fig. 3 Conformable OPVs for energy harvesting with stretchable transparent AgNW/C-PVA/PDMS electrodes. a Schematic diagram of conformable OPV structure. **b** Energy-level diagram of conformable OPVs based on AgNW/C-PVA/PDMS bottom electrodes. **c** *J–V* characteristics of conformable AgNW/C-PVA/PDMS-based OPVs and traditional rigid ITO-based OPV devices. **d** Normalized photovoltaic parameters of conformable OPVs as a function of bending radius (*r*). The inset is the schematic of bending OPVs. **e** Dependence of normalized performance parameters and bending cycles (bending radius of 0.5 mm). The inset is conformable OPVs coiling around a needle. Scale bar is 2 mm.

strain of 72.4%, which met the basic elastic needs of the human body[38,39].

Conformable OPVs with STEs for harvesting energy

Based on the AgNW/C-PVA/PDMS STEs, the conformable OPVs for harvesting energy were fabricated with inverted structure as shown in Fig. 3a. The conformable transparent AgNW/C-PVA/PDMS structure acts as both the bottom transparent electrode and the soft substrate. The typical efficient non-fullerene PM6:Y6 bulk heterojunction (BHJ) is employed here as the active layer of the ultraflexible conformable OPVs. Aluminum-doped zinc oxide (AZO) with the optimized aluminum atomic ratio of 3 at% was adopted as an electron transfer layer (ETL). Compared with traditional zinc oxide (ZnO) ETL, AZO fills the voids among nanowires and helps increase the short-circuit current density (J_{sc}) of the OPVs due to the better conductivity (Supplementary Fig. 3)[40]. The MoO_3 (10 nm)/Ag (100 nm) was evaporated on the active layer as the anode. Figure 3b shows an energy-level diagram of the conformable OPVs. The representative current density-voltage (*J–V*) characteristics of the PM6:Y6-based OPVs with ITO/glass and AgNW/C-PVA/PDMS electrodes under 1 sun illumination are presented in Fig. 3c. The photovoltaic parameters of corresponding devices are summarized in Table 1. For the rigid cells with commercial ITO/glass (R_s of 12 Ω sq^{-1}, T_{avg} of 85%) electrodes show a PCE of 15.8%, an open-circuit voltage (V_{oc}) of 0.83 V, a J_{sc} of 24.9 mA cm^{-2}, and a fill factor of 76.2%. The conformable cells based on AgNW/C-PVA/PDMS STEs (R_s of 18 Ω sq^{-1}, T_{avg} of 90%) show a PCE of 15.2%, a V_{oc} of 0.83 V, a J_{sc} of 25.0 mA cm^{-2}, and a fill factor of 73.2%. The integrated J_{sc} values calculated using the external photovoltaic quantum efficiency (EQE) spectra (Supplementary Fig. 4) were 23.8 and 24.0 mA cm^{-2} for the OPV devices based on the ITO/glass and AgNW/C-PVA/PDMS electrodes, respectively. The results coincided with the J_{sc} measured under the solar simulator with a deviation <5%. It is seen that the performances of conformable OPVs are comparable to those of rigid ITO-based devices and has been at the top level among the reported flexible PM6:Y6 devices with inverted structure[7,41,42].

Table 1. Photovoltaic parameters of OPVs based on ITO/glass and AgNW/C-PVA/PDMS electrodes with typical PM6:Y6 active layer measured under AM 1.5 illumination at 100 mW cm^{-2}.

Electrode	V_{oc} (V)	J_{sc} (mA cm^{-2})	FF (%)	PCE_{max} (PCE_{ave})[a] (%)
ITO/glass	0.83	24.9	76.2	15.8 (15.4 ± 0.3)
AgNW/C-PVA/PDMS	0.83	25.0	73.2	15.2 (14.9 ± 0.2)

[a]The average PCE values were calculated from over 12 devices with standard deviations.

The mechanical robustness and durability of the soft OPVs are evaluated as shown in Fig. 3d, e. The parameters of the conformable OPV devices almost remained unchanged, with an extreme bending radius down to 0.2 mm. The durability of conformable OPV devices was evaluated by employing cyclic bending tests with 4000 cycles at the bending radius of 0.5 mm (Fig. 3e), which is one order of magnitude lower than the most cyclic bending radii applied on the reported flexible OPVs[2,7,19]. The bending strain is estimated as ~3%. The inset presents the optical image of the conformal solar cells coiling around a needle. Moreover, the conformable OPVs based on the STEs retained over

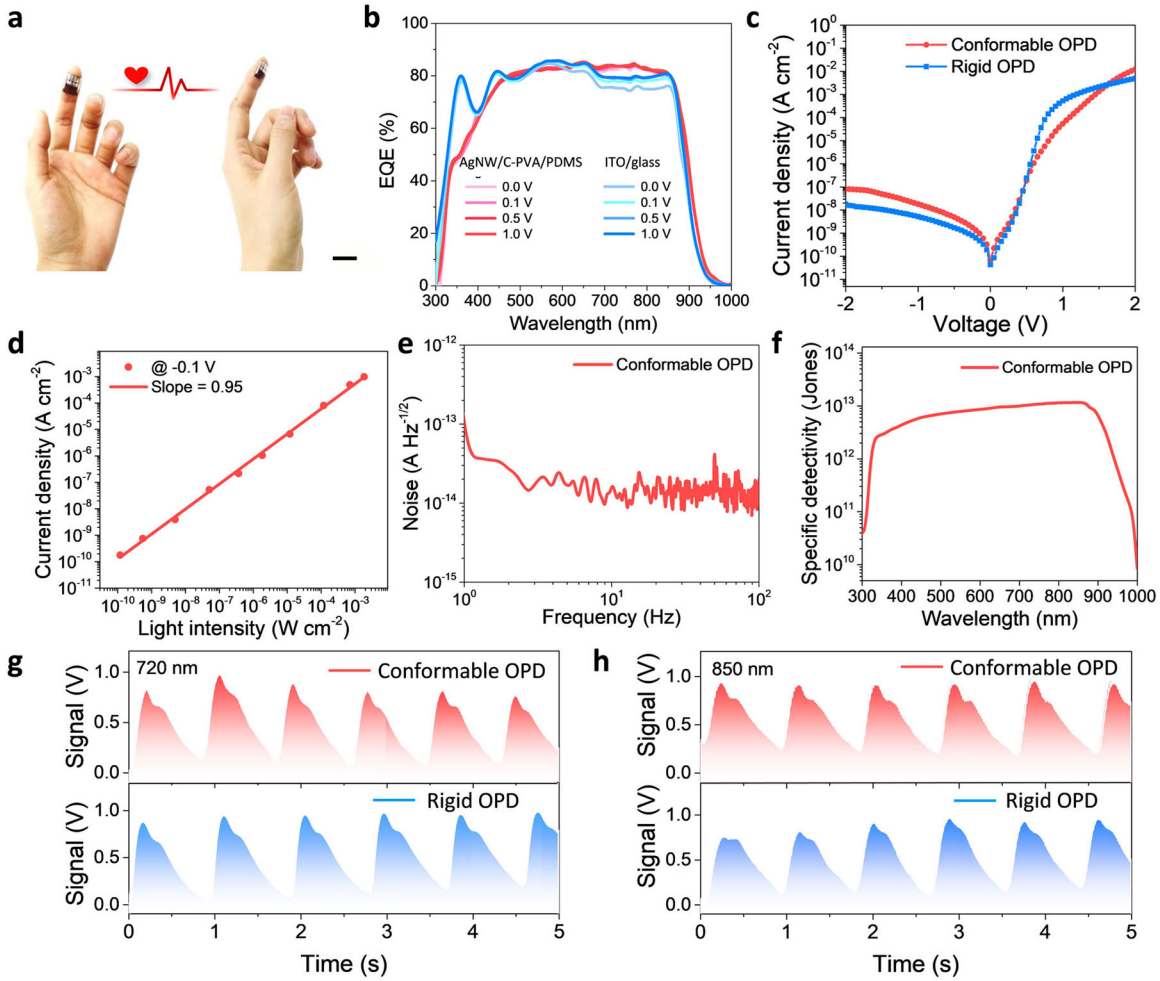

Fig. 4 Conformable wearable OPDs for heart rate detection. a Photographs of conformable OPD devices attached to a finger. Scale bar is 2 cm. **b** EQE curves of the conformable OPDs with AgNW/C-PVA/PDMS electrode and reference rigid device with ITO/glass electrode under 0, 0.1, 0.5, and 1 V bias. **c** Dark current density of conformable OPD and reference rigid device based on PM6/Y6. **d** Linear dynamic range of a conformable OPD under the illumination of 850 nm LED at −0.1 V. **e**, **f** Noise spectral density and specific detectivity for conformable OPD operated under −0.1 V bias. **g**, **h** Signal fluctuations of the conformable and rigid OPDs with the heartbeat under the light of 720 and 850 nm.

96% of their original PCE throughout 4000 bending cycles, demonstrating extraordinary bending durability.

Conformable wearable OPDs with STEs for heart rate detection

Based on the same device structure as depicted above, highly flexible and conformable wearable organic photodetectors were also achieved for real-time heart rate detection as shown in Fig. 4, demonstrating the dual-use capacity of conformable OPV devices. Compared to traditional rigid detecting systems, the conformable photodetectors integrated with light sources are able to monitor heart rate through photoplethysmography (PPG) noninvasively for wearable health and wellness trackers with great convenience and comfort[1]. With the thin and soft AgNW/C-PVA/PDMS electrodes, the skin-like OPDs enable mechanical compatibility with soft tissues, as shown in Fig. 4a, the application for real-time biological signal detection was realized by conformally attaching the OPDs on the finger. Then the underneath incident red or NIR light first penetrates the finger and gets into the conformable photodetector. The transmitted light intensity changes along with the heartbeat due to the changing subcutaneous blood volume, and the electrical signal fluctuation of the detector occurs with the heartbeat[28].

The EQE values of PM6:Y6 photodetectors with AgNW/C-PVA/PDMS and ITO/glass electrodes under different bias voltages are shown in Fig. 4b. Compared with traditional rigid ITO-based devices, the conformable OPDs with AgNW/C-PVA/PDMS electrodes present higher EQE values, especially in the wavelength of 700–900 nm due to the higher transparency of AgNW-based bottom electrodes. For example, the EQE value at 820 nm of the conformable device is 15.2% higher than that of ITO-based devices under the 0 V bias. The conformable devices behave with a very weak dependence on the bias voltage, indicating the efficient charge extraction. The spectral responsivity of the conformable and rigid devices measured under zero bias is shown in Supplementary Note 1 and Supplementary Fig. 5[43]. The peak responsivity of the rigid device is 0.52 A W^{-1} at 850 nm. While the conformable device displays a higher responsivity of 0.54 A W^{-1} at 850 nm benefiting from the improved NIR EQE. The experimental dark current density (J_d) characteristics of OPD devices employing AgNW/C-PVA/PDMS and ITO/glass electrodes are shown in Fig. 4c. It was found that the J_d values for the two devices are comparable (5.9×10^{-10} and 3.3×10^{-10} A cm^{-2} at −0.1 V for AgNW/C-PVA/PDMS and ITO/glass devices, respectively). The ultra-low dark current density and the mechanical conformability of the OPD devices are in favor of achieving high-quality physiological signals for broad utility in biomedical

applications[44]. To investigate the capability of photodetectors operating at a wide range of light intensities, the current density of the conformable device under 850 nm illumination with light intensity ranging from 0.12 nW cm^{-2} to 1.93 mW cm^{-2} are measured (Supplementary Fig. 6). Figure 4d shows that the current density exhibits broad linearity within the test range, and the linear dynamic range (LDR) is calculated as 129 dB (Supplementary Note 2)[45], indicating the good light detect the capability of conformable OPD. Figure 4e shows the measured total noise under −0.1 V bias is frequency-independent at the low-frequency range, and the noise spectral density is around 1.05×10^{-14} A Hz$^{-1/2}$ at 10 Hz, which is close to the calculated noise of 8.7×10^{-15} A Hz$^{-1/2}$. The calculation can be found in Supplementary Note 3, which indicates that the noise is mainly dominated by the shot noise and Johnson noise. As shown in Fig. 4f, the corresponding D^* profiles calculated using the noise current are derived according to Supplementary Note 4. The peak D^* of the conformable OPD reaches 1.67×10^{13} Jones at 850 nm, which is comparable to commercial silicon-based photodiodes[46].

Figure 4g, h shows the electrical signals of the conformal and rigid detectors with heartbeat under the 720 and 850 nm source light. Due to the reduced photon scattering, the sensing of optical signals at 850 nm wavelengths is more distinct for heart rate detection than that measured at 720 nm. At the same source light, the AgNW-based conformable device presents better sensing properties than ITO-based rigid devices, attributing to the high transparency in the NIR region and mechanical conformability. The calculated heart rate values from conformable and rigid OPDs are 69.6 and 67.1 beats per minute, respectively. The heart rate values with acceptable deviation <4% were observed. The demonstration of heart rate sensing highlights a potential application of AgNW-based conformable OPDs in wearable devices.

In summary, the STE made using an AgNW network with a nonuniform Young's modulus structure has a high transmittance in the wide spectrum range, a low sheet resistance, an approaching ideal stretchability, a low surface roughness, and a superior interface wettability. The outstanding characteristics of the STEs enable the fabrication of a highly efficient conformal WOPV device, with high mechanical durability even at an extreme bending radius of 0.5 mm. The PCE of said device, comparable to its ITO analog maintained 96% of it after 4000 bending cycles. Utilizing the same WOPV device architecture, the conformable WOPD was successfully demonstrated for heart rate detection application, indicating STE potential for conformal dual-purpose wearable applications such as health monitoring WOPD and energy-harvesting WOPV device simultaneously, as demonstrated in the study herein. This study paves the way to realize multifunctional WOPV/OPDs that are not only wearable but more importantly, conformable to skin surface seamlessly in the future.

METHODS

Electrode fabrication

A 0.25 wt% AgNW dispersion with a diameter of 30 nm was purchased from Gu' NANO without further treatment. The AgNW dispersion was spin-coated onto the OTS-modified glass substrates, and the solvent was evaporated by annealing at 100 °C for 5 min. The cross-linked PVA was obtained by adding the cross-linking agent glutaraldehyde (Aladdin, 50 wt %) into PVA (Sigma-Aldrich) aqueous solution (6 wt%) with the volume ratio of 1:80. Then, C-PVA was spin-coated on the AgNW network at 7000 rpm for 60 s. The C-PVA substrate was annealed at 100 °C for 1 min on a hot plate to evaporate water. PDMS (Sylgard 184, Dow Corning) was prepared by mixing the base and the cross-linking curing agent in a weight ratio of 10:1, and then was spin-coated at 4000 rpm for 60 s on the C-PVA film, and the PDMS was cured at curing temperature of 100 °C for 5 min. After the PDMS was cured, the AgNW/C-PVA/PDMS embedded electrodes were peeled off from the OTS/glass.

Device fabrication

Conformable OPVs and OPDs were fabricated on the AgNW/C-PVA/PDMS electrodes. First, the free-standing AgNW/C-PVA/PDMS electrode with a thickness of ~30 μm was transferred onto a glass supporting substrate to form a flat surface for further device fabrication. Then, the AZO ETL (40 nm thick) was spin-coated onto the AgNW/C-PVA/PDMS with the spinning rate of 2500 rpm, followed by annealing at 150 °C for 10 min. The optimized sol–gel AZO solution was prepared by dissolving 0.44 g zinc acetate dehydrate, 0.0228 g aluminum nitrate nonahydrate, and 122 μL ethanolamine in 20 mL methoxyethanol. For OPV devices, PM6:Y6 active layer was prepared with a weight ratio of 1:1.2, and was deposited from 6 mg mL^{-1} PM6 concentration in chloroform solution (containing 0.5 vol% chloronaphthalene) at 2700 rpm for 30 s. For OPD devices, PM6:Y6 active layer was optimized with a weight ratio of 1:1.5, and was deposited from 10 mg mL^{-1} PM6 concentration in chloroform solution (containing 0.5 vol% chloronaphthalene) at 2000 rpm for 30 s. The blend film was annealed at 110 °C for 10 min in a glove box. The optimized thickness of PM6:Y6 active layer for OPV and OPD were 89 nm and 290 nm, respectively. The 10 nm MoO_3 HTL and 100 nm Ag anode were thermally evaporated on the active layer through a mask (with a 0.0516 cm^2 area opening) in a vacuum chamber at a base pressure below 1×10^{-6} Pa. Finally, the flexible devices were obtained by peeling off from the supporting substrate. The lamination and delamination process can be found in Supplementary Fig. 7. The reference ITO/glass devices were fabricated with the same conditions.

Device characterization

The sheet resistance of the electrodes was measured using a four-point probe setup. The electrical properties under mechanical deformations were conducted using a lab-made apparatus and Keithley 2450 source meter. Tensile strength and elongation at break were measured with an INSTRON 3300 testing frame. The surface roughness of the embedded electrodes was analyzed by atomic force microscopy (Bruker, Germany). The thickness of the films was determined by a Dektak 150 surface profiler. The *J*–*V* curves of OPVs were performed under standard AM 1.5 G irradiation with a light intensity of 100 mW cm^{-2}. Before the *J*–*V* test, a physical mask of an aperture with a precise area of 0.04 cm^2 was used to define the OPV device area. The EQE spectra were acquired with a Solar Cell Spectral Response Measurement System QE-R3011 (Enlitech Co., Ltd). The light intensity at each wavelength was calibrated using a standard single-crystal Si photovoltaic cell. The J_d–*V* characteristics of the OPD devices were measured on a semiconductor parameter analyzer (Platform Design Automation, PDA FS380 Pro) in an electrically and optically shielded box. The device active area for OPD was 0.0516 cm^2. The noise current from the device was first amplified by the current pre-amplifier (SR 570) and then digitized by a FFT spectrum analyzer (Stanford Research, SR785). The signal response was recorded using a digital oscilloscope (Tektronix TDS3052B). And a current pre-amplifier (Stanford Research, SR 570) was adopted to amplify the input signal and to bias the device simultaneously.

DATA AVAILABILITY

All relevant data that support the findings of this study are available from authors upon reasonable request.

Received: 26 July 2021; Accepted: 13 October 2021;
Published online: 08 November 2021

REFERENCES

1. Jinno, H. et al. Self-powered ultraflexible photonic skin for continuous bio-signal detection via air-operation-stable polymer light-emitting diodes. *Nat. Commun.* **12**, 2234 (2021).
2. Sun, Y. et al. Flexible organic photovoltaics based on water-processed silver nanowire electrodes. *Nat. Electron.* **2**, 513–520 (2019).
3. Kim, J. et al. High performance flexible transparent electrode via one-step multifunctional treatment for Ag nanonetwork composites semi-embedded in low-temperature-processed substrate for highly performed organic photovoltaics. *Adv. Energy Mater.* **10**, 1903919 (2020).
4. Xie, B., Chen, Z., Ying, L., Huang, F. & Cao, Y. Near-infrared organic photoelectric materials for light harvesting systems: organic photovoltaics and organic photodiodes. *InfoMat* **2**, 57–91 (2020).

5. Park, S. et al. Ultraflexible near-infrared organic photodetectors for conformal photoplethysmogram sensors. *Adv. Mater.* **30**, 1802359 (2018).
6. Meng, X. et al. A general approach for lab-to-manufacturing translation on flexible organic solar cells. *Adv. Mater.* **31**, 1903649 (2019).
7. Koo, D. et al. Flexible organic solar cells over 15% efficiency with polyimide-integrated graphene electrodes. *Joule* **4**, 1021–1034 (2020).
8. Qu, T.-Y. et al. Biomimetic electrodes for flexible organic solar cells with efficiencies over 16%. *Adv. Optical Mater.* **8**, 2000669 (2020).
9. Kim, J.-y et al. Low-temperature processable high-performance D-A-type random copolymers for nonfullerene polymer solar cells and application to flexible devices. *Adv. Energy Mater.* **8**, 1801601 (2018).
10. Chen, X. et al. Realizing ultrahigh mechanical flexibility and >15% efficiency of flexible organic solar cells via a "welding" flexible transparent electrode. *Adv. Mater.* **32**, 1908478 (2020).
11. Seo, K.-W., Lee, J., Jo, J., Cho, C. & Lee, J.-Y. Highly efficient (>10%) flexible organic solar cells on PEDOT-free and ITO-free transparent electrodes. *Adv. Mater.* **31**, 1902447 (2019).
12. Wu, H. et al. Electrospun metal nanofiber webs as high-performance transparent electrode. *Nano Lett.* **10**, 4242–4248 (2010).
13. Jeon, I. et al. Direct and dry deposited single-walled carbon nanotube films doped with MoO_x as electron-blocking transparent electrodes for flexible organic solar cells. *J. Am. Chem. Soc.* **137**, 7982–7985 (2015).
14. Song, W. et al. Foldable semitransparent organic solar cells for photovoltaic and photosynthesis. *Adv. Energy Mater.* **10**, 2000136 (2020).
15. Bergqvist, J. et al. Asymmetric photocurrent extraction in semitransparent laminated flexible organic solar cells. *npj Flex. Electron.* **2**, 4 (2018).
16. Tang, H. et al. Highly conducting MXene-silver nanowire transparent electrodes for flexible organic solar cells. *ACS Appl. Mater. Interfaces* **11**, 25330–25337 (2019).
17. Azani, M.-R., Hassanpour, A. & Torres, T. Benefits, problems, and solutions of silver nanowire transparent conductive electrodes in indium tin oxide (ITO)-Free flexible solar cells. *Adv. Energy Mater.* **10**, 2002536 (2020).
18. Fan, X. Doping and design of flexible transparent electrodes for high-performance flexible organic solar cells: recent advances and perspectives. *Adv. Funct. Mater.* **31**, 2009399 (2021).
19. Sun, Y. et al. Flexible high-performance and solution-processed organic photovoltaics with robust mechanical stability. *Adv. Funct. Mater.* **31**, 2010000 (2021).
20. Yan, T. et al. 16.67% rigid and 14.06% flexible organic solar cells enabled by ternary heterojunction strategy. *Adv. Mater.* **31**, 1902210 (2019).
21. Fukuda, K., Yu, K. & Someya, T. The future of flexible organic solar cells. *Adv. Energy Mater.* **10**, 2000765 (2020).
22. Yan, C. et al. Stretchable and wearable electrochromic devices. *ACS Nano* **8**, 316–322 (2014).
23. Liang, J., Tong, K. & Pei, Q. A water-based silver-nanowire screen-print ink for the fabrication of stretchable conductors and wearable thin-film transistors. *Adv. Mater.* **28**, 5986–5996 (2016).
24. Yang, Y. et al. Facile fabrication of stretchable Ag nanowire/polyurethane electrodes using high intensity pulsed light. *Nano Res.* **9**, 401–414 (2016).
25. Yao, S. et al. A wearable hydration sensor with conformal nanowire electrodes. *Adv. Healthc. Mater.* **6**, 1601159 (2017).
26. Xu, J. et al. Highly stretchable polymer semiconductor films through the nanoconfinement effect. *Science* **355**, 59–64 (2017).
27. Chen, Z. H., Fang, R., Li, W. & Guan, J. Stretchable transparent conductors: from micro/macromechanics to applications. *Adv. Mater.* **31**, 1900756 (2019).
28. Xia, Y., Aguirre, L. E., Xu, X. & Inganäs, O. All-polymer high-performance photodetector through lamination. *Adv. Electron. Mater.* **6**, 1901017 (2020).
29. Lochner, C. M., Khan, Y., Pierre, A. & Arias, A. C. All-organic optoelectronic sensor for pulse oximetry. *Nat. Commun.* **5**, 5745 (2014).
30. Armin, A., Vuuren, R. D. J.-v, Kopidakis, N., Burn, P. L. & Meredith, P. Narrowband light detection via internal quantum efficiency manipulation of organic photodiodes. *Nat. Commun.* **6**, 6343 (2015).
31. Wang, S., Oh, J. Y., Xu, J., Tran, H. & Bao, Z. Skin-inspired electronics: an emerging paradigm. *Acc. Chem. Res.* **51**, 1033–1045 (2018).
32. Cui, N. et al. A photolithographic stretchable transparent electrode for an all-solution-processed fully transparent conformal organic transistor array. *J. Mater. Chem. C.* **7**, 5385–5393 (2019).
33. Jeong, S. H., Zhang, S., Hjort, K., Hilborn, J. & Wu, Z. PDMS-based elastomer tuned soft, stretchable, and sticky for epidermal electronics. *Adv. Mater.* **28**, 5830–5836 (2016).
34. Ren, H. et al. High-performance, ultrathin, ultraflexible organic thin-film transistor array via solution process. *Small* **14**, 1801020 (2018).
35. Atkinson, J. & Goldthorpe, I. A. Near-infrared properties of silver nanowire networks. *Nanotechnology* **31**, 365201 (2020).
36. Qin, J. et al. Recent progress in flexible and stretchable organic solar cells. *Adv. Funct. Mater.* **30**, 2002529 (2020).
37. Dagdeviren, C. et al. Conformal piezoelectric systems for clinical and experimental characterization of soft tissue biomechanics. *Nat. Mater.* **14**, 728 (2015).
38. Sun, Z. et al. Skin-like ultrasensitive strain sensor for full-range detection of human health monitoring. *ACS Appl. Mater. Interfaces* **12**, 13287–13295 (2020).
39. Iqbal, S. M. A., Mahgoub, I., Du, E., Leavitt, M. A. & Asghar, W. Advances in healthcare wearable devices. *npj Flex. Electron.* **5**, 9 (2021).
40. Stubhan, T. et al. Inverted organic solar cells using a solution processed aluminum-doped zinc oxide buffer layer. *Org. Electron.* **12**, 1539–1543 (2011).
41. Kim, J. et al. High performance flexible transparent electrode via one-step multifunctional treatment for ag nanonetwork composites semi-embedded in low-temperature-processed substrate for highly performed organic photovoltaics. *Adv. Energy Mater.* **10**, 1903919 (2020).
42. Zhang, W. et al. Graphene:silver nanowire composite transparent electrode based flexible organic solar cells with 13.4% efficiency. *J. Mater. Chem. A* **7**, 22021 (2019).
43. Wang, X. et al. High-performance all-polymer photoresponse devices based on acceptor-acceptor conjugated polymers. *Adv. Funct. Mater.* **26**, 6306–6315 (2016).
44. Jiang, Z. et al. Ultraflexible integrated organic electronics for ultrasensitive photodetection. *Adv. Mater. Technol.* **6**, 2000956 (2020).
45. Zhao, Z., Xu, C., Niu, L., Zhang, X. & Zhang, F. Recent progress on broadband organic photodetectors and their applications. *Laser Photonics Rev.* **14**, 2000262 (2020).
46. Yang, D. & Ma, D. Development of organic semiconductor photodetectors: from mechanism to applications. *Adv. Optical Mater.* **7**, 1800522 (2019).

ACKNOWLEDGEMENTS

This work was financially supported by the National Key Research and Development Program of China (No. 2019YFA0705900) funded by MOST, the Basic and Applied Basic Research Major Program of Guangdong Province (No. 2019B030302007), the National Natural Science Foundation of China (No. 51521002), and Guangdong-Hong Kong-Macao joint laboratory of optoelectronic and magnetic functional materials (No. 2019B121205002).

AUTHOR CONTRIBUTIONS

F.H. and N.C. conceived and designed the work. N.C. carried out conformable device fabrication and performed electrical and optical measurements. Y.S. and N.C. conducted characterization of OPD characterization and implemented heart rate detecting. F.H., C.N., and C.-H.T. wrote and revised the manuscript. K.Z., X.Y., S.D., and B.X. analyzed and interpreted the data. All authors discussed the results and commented on the final manuscript. F.H. supervised the project.

COMPETING INTERESTS

The authors declare no competing interests.

ADDITIONAL INFORMATION

Supplementary information The online version contains supplementary material available at https://doi.org/10.1038/s41528-021-00127-7.

Correspondence and requests for materials should be addressed to Fei Huang.

Reprints and permission information is available at http://www.nature.com/reprints

Publisher's note Springer Nature remains neutral with regard to jurisdictional claims in published maps and institutional affiliations.

Open Access This article is licensed under a Creative Commons Attribution 4.0 International License, which permits use, sharing, adaptation, distribution and reproduction in any medium or format, as long as you give appropriate credit to the original author(s) and the source, provide a link to the Creative Commons license, and indicate if changes were made. The images or other third party material in this article are included in the article's Creative Commons license, unless indicated otherwise in a credit line to the material. If material is not included in the article's Creative Commons license and your intended use is not permitted by statutory regulation or exceeds the permitted use, you will need to obtain permission directly from the copyright holder. To view a copy of this license, visit http://creativecommons.org/licenses/by/4.0/.

© The Author(s) 2021